

NUMERICAL MODEL AND EFFICIENCY ANALYSIS OF FINNED STAGGERED SOLAR PV/T AIR COLLECTOR

Rundong Zhang, Liang Pan, Dali Ding, Jianrui Bai, Weijian Zhang, and Qi Du*

College of Energy and Power Engineering, Changchun Institute of Technology, Changchun 130012, Jilin, China

*Corresponding Author: Liang Pan. Email: nd_pl@ccit.edu.cn

This paper introduces a novel design for a solar PV/T air collector that utilizes staggered fins. The collector features double-layer flow channels in the same direction, with the upper channel equipped with transparent wave plates, and the lower channel fitted with staggered fins. The paper includes a calculation scheme for wave plate heat balance. The numerical model of the collector is established and verified by experimental results. A numerical model is used to analyze the height combination of the upper and lower runner and the fin arrangement of the lower runner. The results indicate that, under the given environmental parameters, as the photovoltaic panel moves down, the overall air heat transfer capacity decreases. When the height combination of the upper/lower runner is 23mm/105mm, the maximum value is 53.741%. With the increase of fin spacing, the heat transfer capacity of the lower runner decreases. With the increase of the number of fin rows, the heat transfer capacity of the lower runner increases. When the equivalent diameter of the rectangular channel and the number of fin rows were 70mm and 3 rows, respectively, the maximum solar energy comprehensive utilization efficiency was 56.261%.

Key words: PV/T collector, Enhanced heat transfer, efficiency, Solar energy, Numerical simulation

1 Introduction

In 1978, Kern and Russell^[1] proposed a solar photovoltaic/thermal (PV/T) collector that combines photovoltaic power generation and solar thermal utilization. The fluid in the collector takes away the heat energy, which effectively reduces the temperature of the solar cell, and the power generation performance of the solar cell is improved. This significantly improves the overall utilization efficiency of solar energy. This approach enables the supply of both electric energy and heat energy simultaneously^[2-4].

Based on the cooling methods, the solar PV/T collector can be categorized into four forms: air cooling, water cooling, refrigerant cooling, and heat pipe cooling^[5]. Among these cooling methods, the solar PV/T air collector offers several advantages, including low cost, easy installation, and no need for anti-freezing measures during winter^[6]. However, the low specific heat capacity of air and small temperature difference for heat transfer between air and solar cells limit the heat transfer capacity of the solar PV/T air collector^[7-8]. Therefore, optimizing the structure of the solar PV/T air collector to enhance the heat transfer capacity between air and photovoltaic panels has become a major research focus in this field. In the process of optimizing the solar PV/T air collector's structure, the flow channel form, fin structure, and arrangement are key factors for improving the heat transfer

capacity between air and photovoltaic panels.

The impact of channel form on heat transfer capacity lies in increasing the heat transfer area and prolonging the heat transfer time per unit volume of air. The primary flow channel forms include single-channel, double-channel, and double-layer single-channel, among which the double-channel solar PV/T air collector exhibits better performance. Kamthania et al.^[9] established a mathematical model and found that, under the climate of New Delhi, India, the air outlet temperature of a two-channel solar PV/T collector was 3–4°C higher than that of a single-channel solar collector. Mohamed El Amine Slimani et al.^[10] analyzed the performance of single-channel and double-layer single-channel solar PV/T collectors and discovered that the solar cell temperature in the double-channel PV/T collector was 11°C lower than that in the single-channel PV/T collector. Poorya Ooshaksaraei et al.^[11] conducted experimental research on four kinds of solar PV/T collectors, including single-channel, double-channel coflow, double-channel countercurrent and double-layer single-channel. The total efficiency was found to be 28% - 49%, 51% - 67%, 47% - 62% and 42% - 56%, respectively.

The optimization of the fin structure and arrangement can improve the heat transfer coefficient by changing the air flow state, enhancing the disturbance in the boundary layer, and reducing the thickness of the flow boundary layer^[12]. Elsafi and Gandhidasan^[13] increased the number of fins from 10 to 50 in a two-channel solar PV/T collector through a mathematical model. As a result, the surface temperature of solar cells decreased from 43°C to 36°C, and the photoelectric conversion efficiency increased by about 2%. Juwel Chandra Mojumder et al.^[14] found that increasing the number of fins in a single-channel solar PV/T collector improved its performance, with photoelectric/photothermal conversion efficiency of 13.75% and 56.19%, respectively. Hwi-Ung Choi et al.^[15] used unequal cross-section fins in a two-channel solar PV/T collector to enhance the gas disturbance, which resulted in photoelectric/photothermal conversion efficiency of 14.81% and 56.72%, respectively. Ji-Suk Yu et al.^[16] arranged triangular baffles on the upper side of the thermal insulation backplane of a single-channel solar PV/T collector, which increased the temperature of the solar PV/T collector outlet by 3.6–3.9°C and increased photothermal conversion efficiency by 31%. Prabhakar Jha et al.^[17] used a wave-type insulation backplane in a single-channel solar PV/T collector, which enhanced the disturbance to the air and resulted in a photothermal conversion efficiency of 8.4% higher than that of the single-channel solar PV/T collector with a flat-type insulation backplane.

In order to effectively improve the efficiency of a solar PV/T air collector, a double-channel design with staggered fins is proposed in this paper, based on the two main factors mentioned above. The system features a double-layer runner where the air flows in the same direction, with a transparent wave plate installed in the upper runner to enhance the disturbance in the gas flow process, while the lower runner has staggered fins to increase the air heat transfer area and reduce the overall thickness of the flow boundary layer. This paper establishes a numerical model of the collector and verifies the simulation results by comparing them with experimental data. Finally, the structure of the collector is analyzed and optimized through numerical study, focusing on the upper/lower runner height combination and lower runner fin arrangement, then compared with other collectors. The main objectives of this work are to: (1) propose a new solar PV/T air collector structure design; (2) add the wave plate heat balance calculation scheme and establish a numerical model of the collector; (3) verify the accuracy of the solar PV/T collector numerical model through experiments under natural weather conditions; and (4) analyze the influence of different structural parameters on the collector efficiency and search for optimization.

2 Experimental system

2.1 Solar collector configuration

The fig.1 in this paper shows the solar PV/T air collector. The collector modules, from top to bottom, consist of a glass cover plate, a transparent wave plate, a photovoltaic panel (including a solar cell and heat-absorbing

plate), fins, and a insulation backboard.

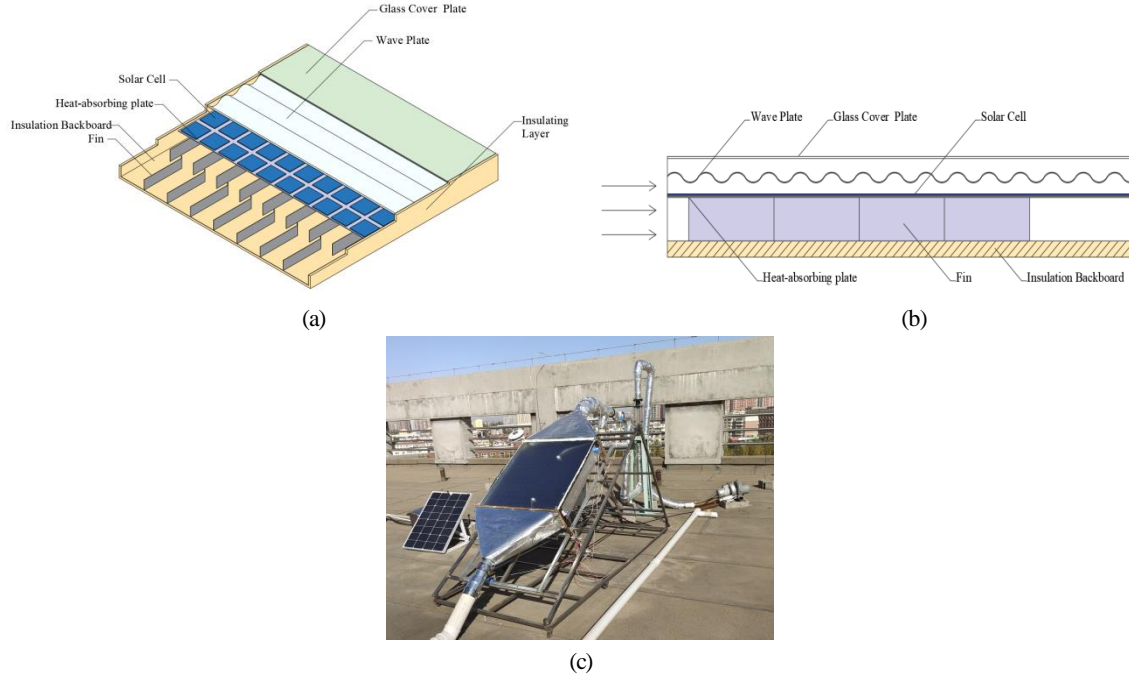


Fig.1 Solar PV/T air collector: (a) Collector structure drawing; (b) Collector side view; (c) Collector physical picture.

The collector is composed of a glass cover plate, insulation backboard, and thermal insulation board on both sides of the external frame. The photovoltaic plate is positioned in the middle of the collector, and the transparent wave plate is arranged on the photovoltaic plate to create an upper flow channel. The trough of wave plate is 0.02 m away from the upper surface of the photovoltaic plate. The photovoltaic plate and the thermal insulation backplane create a lower flow channel with a height of 0.1 m, and the fins are staggered in the lower flow channel. The glass cover plate is made of double-layer vacuum 3.2 mm thick toughened glass with super white cloth pattern, and the transparent wave plate is made of polycarbonate material. The thermal insulation backplane and side thermal insulation panels are 0.015 m rubber and plastic thermal insulation materials.

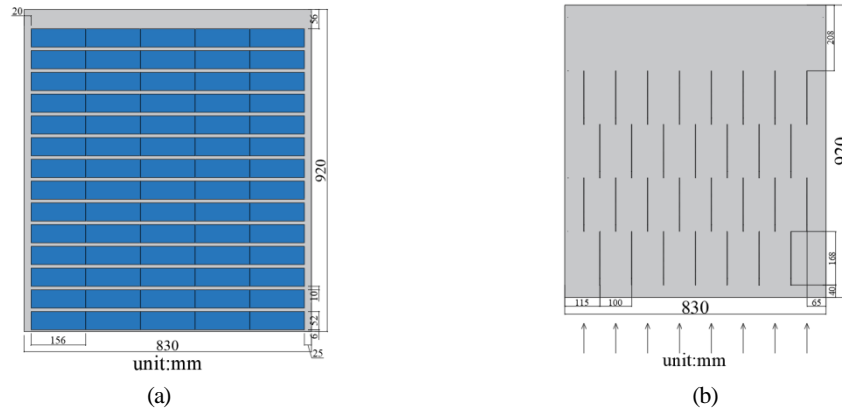


Fig.2 Photovoltaic panel structure: (a) Solar cell arrangement; (b) Finned arrangement.

The photovoltaic panel structure is shown in fig.2. The photovoltaic panel is 0.92m long and 0.83m wide. The photovoltaic panel is made up of 70 monocrystalline silicon solar cells that are 0.156m long and 0.052m wide. The total area of the solar cells is 0.568m², and the coverage ratio (ζ) is 75.46%. The panel has a reference photoelectric conversion efficiency (η_{ref}) of 7.87% under standard test conditions of a temperature (T_{ref}) of 291.84K, solar radiation of 1000W/m², and wind speed of 0m/s. The temperature coefficient Br is 0.0045K⁻¹. The lower side of the photovoltaic panel has an absorption plate composed of two layers of selective absorption film and aluminum plate, with the absorption film made of reduced graphene oxide. The back of the heat-absorbing plate has four rows of ribs, with 7-8 pieces in each row, staggered in arrangement. Each rib is made of metal plates with high thermal conductivity, with a length of 168mm and a height of 100mm. Table 1 summarizes the

main characteristics of each component of the solar PV/T collector.

Table 1. Main characteristics of each component of solar PV/T air collector

Properties	Glass cover plate	Wave plate	Solar cell	Heat-absorbing plate	Fins	Insulation backboard
Emissivity ε	0.9	0.91	0.7	-	-	-
Absorptance α	0.0094	0.001	0.7614	-	-	-
Transmittancy τ	0.9201	0.85	-	-	-	-
Thickness H (m)	3.2×10^{-3}	1×10^{-3}	1×10^{-3}	0.3×10^{-3}	0.1	15×10^{-3}
Density ρ (kg/m ³)	2.6×10^3	1.38×10^3	2.34×10^3	7.85×10^3	7.85×10^3	5.47×10^3
Specific heat c (kJ/(kg·k))	0.837×10^3	1.26×10^3	0.7×10^3	0.46×10^3	0.46×10^3	1.2×10^3

2.2 Experimental cases

The experimental platform was built in Changchun, Jilin Province of China. The system is mainly composed of solar PV/T collector, ventilation pipe, blower, float flowmeter, sensor and other components. The solar collectors was kept stationary, facing to the south with an angle of 30° to the ground. The experiment time is usually from 9:00 to 15:00. Due to the low temperature at night, the initial temperature of the collector components is low, and the solar collector is pre-run for half an hour from 8:30. After the start of the experiment, the air flow was maintained at 0.0075kg/s, and the temperature of each component, voltage of photovoltaic panel and current of photovoltaic panel changes were recorded by the sensor.

2.3 Uncertainty analysis

To ensure the accuracy of the experimental results, we conducted an uncertainty analysis. The uncertainty analysis of the experimental results is calculated by the following equation[18].

$$W_R = \left[\left(\frac{\partial R}{\partial x_1} w_1 \right)^2 + \left(\frac{\partial R}{\partial x_2} w_2 \right)^2 + \cdots + \left(\frac{\partial R}{\partial x_n} w_n \right)^2 \right]^{0.5} \quad (1)$$

where W_R denotes the uncertainty, R is a given function of independent variables (x_1, x_2, \dots, x_n), and w_1, w_2, \dots, w_n denote the uncertainties of x_1, x_2, \dots, x_n .

The uncertainty of the experimental results is mainly due to the uncertainty of the measurement results of solar irradiance, current and voltage, and air inlet and outlet temperature. Qualitatively related. The uncertainty distribution of thermal/electrical efficiency and solar comprehensive efficiency calculated from the accuracy of experimental instruments shown in tab.2 are 2.56%, 0.22% and 2.99%. The results show that the uncertainty of experimental test is less than 3%, and the experimental accuracy is guaranteed.

Table 2. Parameters of experimental instruments

instrument	precision	range	model
Ambient temperature and humidity sensor	$\pm 0.5^\circ\text{C}$ 、 $\pm 3\%\text{RH}$	$-40 \sim 80^\circ\text{C}$ 、 $0 \sim 100\%\text{RH}$	PR-300BYH-M
Radiation sensor	$\pm 2\%$	$0 \sim 2000\text{W/m}^2$	TBQ-2
Thermal resistance sensor	$\pm 0.3^\circ\text{C}$	$-50 \sim 100^\circ\text{C}$	PT100
Current sensor	$\pm 0.2\%$	$0 \sim 20\text{A}$	YDG-HTD-4
Voltage sensor	$\pm 0.1\%$	$0 \sim 75\text{V}$	VDT-21
Float flowmeter	$\pm 1.5\%$	$12 \sim 120\text{m}^3/\text{h}$	LZB-40
Data acquisition instrument	-	-	DAM3158A

3 Establishment of numerical model

3.1 Energy balance equation of each component

Drawing upon existing solar PV/T collector heat transfer models outlined in literature^[19-21], this paper develops a novel finned staggered solar PV/T air collector heat transfer model. Figure 3 describes the heat transfer process of the solar PV/T air collector, and the energy balance equation of each component is established

according to the heat transfer process.

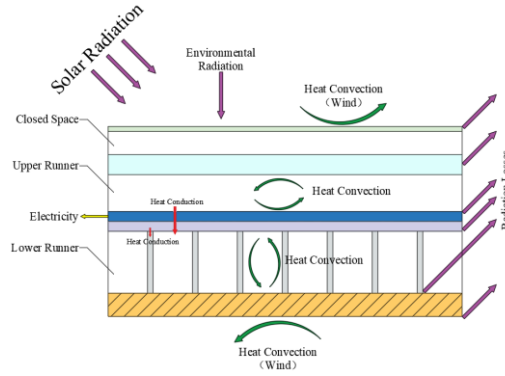


Fig.3 Front view of solar PV/T collector heat transfer model

The following assumptions were made in establishing the model:

- (1) The thermal and physical properties of photovoltaic cells remain constant throughout the simulation;
- (2) The solar irradiance is uniformly distributed across the surface of the collector;
- (3) The temperature of each component is evenly distributed;
- (4) The side walls of the collector are considered to be adiabatic;
- (5) The fluid (air) does not participate in radiation exchange, and only the temperature change along the flow direction is taken into account;
- (6) The top and bottom surfaces of the collector are exposed to the same ambient temperature and wind speed.

3.1.1 Glass cover plate

The heat transfer of the glass cover includes heat transfer with the external environment, heat transfer with the sky through radiation, radiation and convection heat transfer with the wave plate, and absorption of solar radiation.

$$M_g c_g \frac{dT_g}{dt} = A_g h_a (T_a - T_g) + A_g h_{e,g} (T_e - T_g) + A_g h_{g,w} (T_w - T_g) + A_g G \alpha_g \quad (2)$$

Where, T_a is the ambient temperature [K], T_g is the temperature of the glass cover [K], T_w is the temperature of the waved plate [K], T_e is the equivalent sky temperature [K], A_g is the area of the glass cover [m²], h_a is the convective heat transfer coefficient between the glass cover and the ambient air [Wm⁻²K⁻¹], $h_{e,g}$ is the radiant heat transfer coefficient between the glass cover and the sky [Wm⁻²K⁻¹], $h_{g,w}$ is the radiant heat transfer coefficient between the glass cover and the wave plate [Wm⁻²K⁻¹], G is the solar irradiance [Wm⁻²], α_g is the absorption ratio of the glass cover to the solar radiation.

Convective heat transfer coefficient between glass cover plate and ambient air is affected by ambient wind speed^[22]. The formula is as follows:

$$h_a = 2.8 \cdot v_a^3 \quad (3)$$

Where, v_a is the ambient wind speed [m/s].

3.1.2 Waved plate

The energy balance equation of the wave plate includes various internal energy changes. These changes are attributed to radiation and convective heat transfer between the glass cover plate, radiation and convective heat transfer between the solar cell layer, and convective heat transfer between the upper flow passage air.

$$M_w c_w \frac{dT_w}{dt} = A h_{g,w} (T_g - T_w) + A h_{w,p} (T_p - T_w) + A h_{w,f} (T_f - T_w) + A G \alpha_w \tau \quad (4)$$

Where, T_{pv} is the temperature of the solar cell layer [K], T_{fl} is the air temperature of the upper passage [K],

h_{wPV} is the radiative heat transfer coefficient between the wave plate and the solar cell layer [$\text{Wm}^{-2}\text{K}^{-1}$], A_w is the area of the wave plate [m^2], h_{wfl} is the convective heat transfer coefficient between the wave plate and the air of the upper passage [$\text{Wm}^{-2}\text{K}^{-1}$], α_w is the absorption ratio of the wave plate to the solar radiation, τ_g is the transmission ratio of the glass plate to the solar radiation.

The wave plate in question has a wavy shape, causing the cross-sectional area of the airflow channel to fluctuate continuously as the air flows through it. This fluctuation impedes the accurate assessment of the air flow state and hinders the calculation of the convective heat transfer coefficient (h_{wfl}) between the air and the aforementioned surfaces. To surmount this challenge, we resort to the integration of the wave plate's trajectory equation to determine the average Reynolds number of the fluid in the upper flow passage. Along the direction of air flow, we establish a coordinate system with the air inlet as the origin and the upper side of the photovoltaic panel as the x -axis to derive the wave plate trajectory equation $f(x)$. The resulting equation for the integral average height (H_1) of the upper runner reads as follows:

$$f(x) = 0.008 \frac{\pi x}{0.031} + 0.0015 \quad (5)$$

$$H_1 = \frac{\int_0^l f(x) dx}{l} \quad (6)$$

Where, H_1 is the average integrated height of the upper runner [m], $f(x)$ is the trajectory equation of the wave plate, and l is the length of the runner [m].

At this time, the equation to calculate the average Reynolds number of the upper runner is as follows[23]:

$$Re_{f1} = \frac{\frac{Q_{f1}}{H_1 \times b_{f1}} \times D_{f1}}{\nu} \quad (7)$$

Where, Re_{f1} is the air Reynolds number of the upper passage, Q_{f1} is the air flow rate of the upper passage [m^3s^{-1}], b_{f1} is the width of the upper passage [m], D_{f1} is the equivalent diameter of the upper passage [m], ν is the viscosity coefficient of air motion [m^2s^{-1}].

Wherein, the equivalent diameter D_{f1} is calculated by the following formula:

$$D_{f1} = 4 \times \frac{H_1 \times b_{f1}}{2 \times (H_1 + b_{f1})} \quad (8)$$

Then, according to the calculated average Reynolds number, the convective heat transfer coefficient h_{wfl} can be calculated by Nu number. λ is the thermal conductivity of air, the calculation formula is as follows[24-26]:

$$Nu_{fi} = 1.86 Re_{fi}^{\frac{1}{3}} Pr_{fi}^{\frac{1}{4}} \left(\frac{D_{fi}}{l_{fi}} \right)^{-\frac{1}{3}} \frac{\mu_w}{\mu} \quad (9)$$

$$h_{w,f1} = \frac{Nu_{f1} \times \lambda}{D_{f1}} \quad (10)$$

Where, when $i = 1$ is the upper flow passage, when $i = 2$ is the lower flow passage, Nu_{fi} is the Nusselt number of air, Pr_{fi} is the Prandtl number of the upper runner, μ_{fi} is the dynamic viscosity of air at the average air temperature [$\text{Pa}\cdot\text{s}$], and μ_w is the dynamic viscosity of air at the flow wall temperature [$\text{Pa}\cdot\text{s}$], λ is heat conductivity coefficient [$\text{W}/(\text{m}\cdot\text{K})$].

3.1.3 Solar cell

The energy balance equation for the solar cell layer is a complex function of various internal energy changes. These changes arise from a combination of radiation and convective heat transfer between the wave plate, heat conduction between the absorption plate, convective heat transfer between the air in the upper flow passage, solar

radiation absorption, and the solar cell's electrical output.

$$M_{PV} c_{PV} \frac{dT_{PV}}{dt} = A_{PV} h_{w,PV} (T_w - T_{PV}) + A_{PV} h_{p,PV} (T_p - T_{PV}) + A_{PV} h_{PV,f} (T_f - T_{PV}) + A_{PV} \tau_w \tau_g \alpha_{zh} G - \xi A_{PV} E_{PV} \quad (11)$$

Where, T_p is the temperature of the absorption plate [K], α_{zh} is the actual absorption ratio of solar radiation of the solar cell layer, A_{PV} is the area of the solar cell layer [m^2], $h_{p,PV}$ is the heat transfer coefficient between the solar cell layer and the absorption plate [$Wm^{-2}K^{-1}$], $h_{PV,f}$ is the convective heat transfer coefficient between the solar cell layer and the air in the upper flow passage [$Wm^{-2}K^{-1}$], τ_w is the transmission ratio of the solar radiation to the wave plate, E_{PV} is the output power of the solar cell [Wm^2].

Since the solar cell coverage ratio ξ is not up to 100%, and the rest of the solar radiation is received by the selective absorption film, it is necessary to calculate the actual absorption rate of solar radiation of the solar cell layer, the calculation formula is as follows[27]:

$$\alpha_{zh} = \xi \alpha_{PV} + (1 - \xi) \alpha_x \quad (12)$$

Where, α_{PV} is the absorption ratio of solar radiation to solar cell, and α_{xsm} is the absorption ratio of solar radiation to selective absorption film.

The calculation of output power of E_{PV} for solar cells shall be carried out according to the factory parameters of solar cells^[28], and the calculation formula is as follows:

$$E_{PV} = G \eta \left[1 - B(T_{PV} - T_{ref}) \right] \quad (13)$$

Where, E_{PV} is the instantaneous power output of the solar cell [Wm^2], η_{ref} is the reference photoelectric conversion efficiency of the solar cell, Br is the temperature coefficient [K^{-1}], T_{PV} is the surface temperature of the solar cell [K], and T_{ref} is the test temperature of the solar cell [K].

3.1.4 Heat-absorbing plate

The heat transfer model for the endothermic plate incorporates several heat transfer mechanisms. These include heat conduction between the endothermic plate and the solar cell layer, heat conduction between the endothermic plate and the lower fins, convective heat transfer between the endothermic plate and the air in the lower flow passage, and radiation heat transfer between the endothermic plate and the thermal insulation backplane. Notably, the primary heat transfer mode between the endothermic plate and the thermal insulation backplane is radiation heat transfer. The corresponding energy balance equation is articulated as follows:

$$M_p c_p \frac{dT_p}{dt} = A_{p,p} h_{p,p} (T_w - T_p) + A_{p,l} \lambda \frac{T_{fin} - T_p}{\frac{1}{h_{p,l}} + \frac{H_{fin}}{2}} + A_{p,i} h_{p,i} (T_2 - T_p) + A_{p,b} \epsilon_p \sigma (T_b^4 - T_p^4) \quad (14)$$

Where, T_{fin} is the fin temperature [K], T_2 is the air temperature of the lower flow passage [K], T_b is the temperature of the insulation backplane [K], H_{fin} is the fin height [m], A_p is the area of the endothermic plate [m^2], $A_{p,l}$ is the contact area between the endothermic plate and a single fin [m^2]. n is the number of fins, h_p ; b is the radiant heat transfer coefficient between the endothermic plate and the insulation backplane [$Wm^{-2}K^{-1}$]; $h_{p,l}$ is the convective heat transfer coefficient between the endothermic plate and the air in the lower flow passage [$Wm^{-2}K^{-1}$]; λ_{fin} is the thermal conductivity coefficient between the endothermic plate and the fin [$Wm^{-1}K^{-1}$].

Due to the staggered configuration of fins in the lower channel, the air is constantly redistributed to regenerate the boundary layer in the subsequent rectangular channel. Therefore, the lower channel can be divided into a combination of several rectangular channels. From this perspective, the convective heat transfer coefficient, denoted as $h_{p,l}$ between the heat-absorbing plate and the air in the lower runner can be derived by applying the following formula:

$$h_{p,f2} = \frac{Nu_{f2} \times \lambda}{D_{f2}} \quad (15)$$

Where, Nu_{f2} is the Nusselt number of air in the lower runner, and D_{f2} is the equivalent diameter of the rectangular runner composed of the endothermic plate, fin and thermal insulation backplane [m].

Nu_{f2} of the air in the lower runner can be calculated according to equations (8), where the equivalent diameter D_{f2} of the rectangular runner and the air Reynolds number Re_{f2} of the lower runner are calculated as follows:

$$D_{f2} = 4 \times \frac{H_2 \times b_p}{2 \times (H_2 + b_p)} \quad (16)$$

$$Re_{f2} = \frac{\frac{Q_{f2}}{H_2 \times b_p} \times D_{f2}}{v} \quad (17)$$

Where, H_2 is the height of the lower runner [m], b_p is the fin spacing [m], and Q_{f2} is the air flow of the lower runner [$m^3 s^{-1}$].

3.1.5 Fin

The energy balance equation of the fin involves the internal energy changes resulting from the heat conduction between the fin and the heat-absorbing plate, as well as the convective heat transfer that occurs with the air in the lower runner. To calculate this equation, the following formula is utilized:

$$nM_{fin} \frac{dT_{fin}}{dt} = nA \left[\lambda_p \frac{T_p - T_{fin}}{H_{fin}} - h_{f2} (T_{fin} - T_{f2}) \right] \quad (18)$$

Where, A_{fin} is the fin area [m^2], h_{f2} is the convective heat transfer coefficient between the fin and the air in the lower passage [$W m^{-2} K^{-1}$].

3.1.6 Insulation backboard

The transfer of heat through the insulation backplane involves several mechanisms, including convective heat transfer between the backplane and the air in the lower runner, radiative heat transfer between the backplane and the endothermic plate, and heat loss due to the temperature differential between the backplane and the surrounding environment.

$$M_b c_b \frac{dT_b}{dt} = A_b \left[h_{b2} (T_{f2} - T_b) + u_b (T_p - T_b) + A_{\epsilon} \epsilon (T_p - T_b) \right] \quad (19)$$

Where, A_b is the area of the insulation backplane [m^2], h_{b2} is the convective heat transfer coefficient between the insulation backplane and the air in the lower flow passage [$W m^{-2} K^{-1}$], u_b is the heat loss of the insulation backplane to the environment [$W m^{-2} K^{-1}$].

$$u_b = \frac{1}{\frac{1}{h_a} + \frac{d_R}{\lambda_R}} \quad (20)$$

Where, λ_R is thermal conductivity of insulation layer [$W m^{-1} K^{-1}$], and d_R is thickness of insulation layer [m].

3.1.7 Air

The following formula is the energy conservation equation of the air in the upper/lower runner:

$$c_{f1} \dot{m}_{f1} \Delta l \frac{dT_{f1}}{dl_{f1}} = A \left[h_w (T_{f1} - T_w) + h_{p1} (T_p - T_{f1}) \right] \quad (21)$$

$$c_{f2} \dot{m}_f \Delta l_f \frac{dT_{f2}}{dl_{f2}} = A h_p (T_{f2} - T_{f1}) \quad (22)$$

Where, c_{f1} and c_{f2} are specific heat of air on/under the flow passage [kJ/(kg·K)], \dot{m}_{f1} and \dot{m}_{f2} for up/down the quality of the air flow in the runner [kg/s], Δl_{f1} and Δl_{f2} for up/down flow length [m].

The average air temperature of the upper and lower runner is given by the following formula:

$$T_{fi} = \frac{T_{fi,in} + T_{fi,out}}{2} \quad (23)$$

$$\frac{dT_{fi}}{dl_{fi}} = \frac{T_{fi,in} - T_{fi,out}}{\Delta l_{fi}} \quad (24)$$

Where, T_{fi} is the average air temperature [K], $T_{fi,in}$ is the air inlet temperature [K], $T_{fi,out}$ is the air outlet temperature [K].

3.2 Performance Evaluation

3.2.1 Evaluation parameters of heat transfer capacity

The strength of air heat transfer capacity in the upper passage is influenced by the disturbance intensity J of the air caused by the wave plate. This intensity, in turn, is dependent on the distance between the wave peak height H_{bf} and the wave trough height H_{bg} , as illustrated in fig.4.

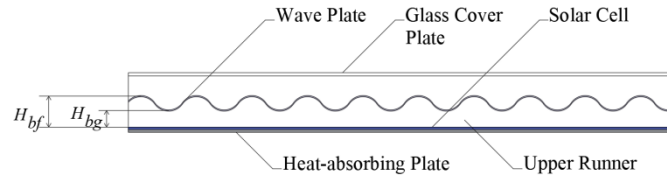


Fig.4 Schematic diagram of upper runner

When the wave plate is situated infinitely far away from the solar cell, the peak and trough heights tend to be equal, resulting in a disturbance intensity of approximately 1. However, as the wave plate approaches the solar cell, the trough height approaches 0^[29]. To evaluate air heat transfer capacity, the disturbance intensity J is employed as the key parameter, calculated using the following formula:

$$J = \frac{H_{bf}}{H_{bg}} \quad (25)$$

Where, J is the disturbance intensity, H_{bf} is the crest height of wave plate [m], and H_{bg} is the trough height of wave plate [m].

The staggered arrangement of fins plays a pivotal role in enhancing the air heat transfer capacity in the underflow passage. The critical parameters of this arrangement include the fin spacing and the number of fin rows. Equations (14)-(16) illustrate that altering the fin spacing leads to a change in the equivalent diameter D_{f2} of the rectangular runner, which, in turn, influences the air Reynolds number Re_{f2} in the lower runner and improves the air heat transfer capacity. Additionally, the number of fin rows (z) has a significant impact on the heat transfer capacity of the lower runner. To be precise, z is defined as the ratio of the total length of the runner (l) to the length (l_p) of the fin. The corresponding calculation formula is given as follows:

$$z = \frac{l}{l_p} \quad (26)$$

Where, z is the number of fin rows, l is the total length of runner [m], l_p is the length of fin [m]. By evaluating air heat transfer capacity with these parameters, a more precise and accurate analysis of the heat transfer process can be obtained.

3.2.2 Conversion efficiency evaluation parameter

The thermoelectric performance of the system can be calculated by the photothermal conversion efficiency η_{th} , photoelectric conversion efficiency η_{PV} and solar comprehensive utilization efficiency η_f . Instantaneous photothermal conversion efficiency is defined as the ratio of the heat gained by the air to the solar radiation projected onto the collector:

$$\eta_{th} = \frac{\dot{m}c_{ap}(T_{out} - T_{in})}{GA_c} \quad (27)$$

Where, \dot{m} as air mass flow rate [kg/s], c_{ap} for air specific heat at constant pressure [J/(kg·K)], T_{in} and T_{out} as the air temperature at the inlet and outlet of the collector [K], A_c for collectors lighting area [m²].

Photovoltaic conversion efficiency of solar PV/T collector is defined as the ratio of the total energy generated by the collector to the total solar radiation projected onto the collector:

$$\eta_{PV} = \frac{\sum UI}{GA_{PV}} \quad (28)$$

Where, U is the collector output voltage [V], I is the collector output current [A], A_{PV} is the total area of the solar cell [m²].

Since electric energy is a higher grade energy than thermal energy, in order to fairly evaluate the performance of solar PV/T collector, its solar comprehensive utilization efficiency is defined as^[30]:

$$\eta_f = \eta_{th} + \xi \frac{\eta_{PV}}{\eta_{power}} \quad (29)$$

Where, η_{power} refers to the generating efficiency of thermal power plants (38%).

3.3 Solution method for model

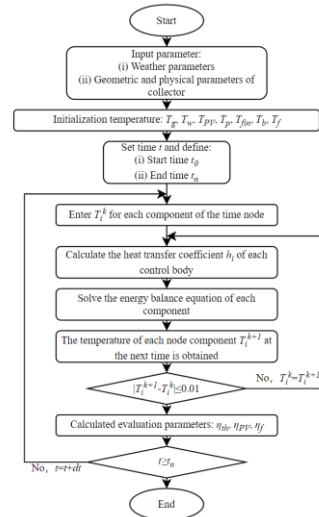


Fig.5 Model solving flow chart

The model solving process is illustrated in fig.5. In light of the boundary conditions provided and the heat transfer coefficient calculation formula, a simulation program has been developed to iteratively solve the energy balance equation and determine the temperature of the solar PV/T air collector component, photothermal/photoelectric conversion efficiency, and solar energy comprehensive utilization efficiency.

3.4 Model validation

The operational parameters used for verification were derived from experimental data collected on March 8, 2022, in Changchun, Jilin Province, China. The experiment was conducted between 9:00 a.m. and 3:00 p.m., during which the average ambient temperature was 5.91°C, the total solar radiation was 13.66 MJ/m², and the air

flow rate in the collector was 0.0075 kg/s. Hourly changes in total solar radiation, ambient temperature, and ambient wind speed are depicted in fig.6.

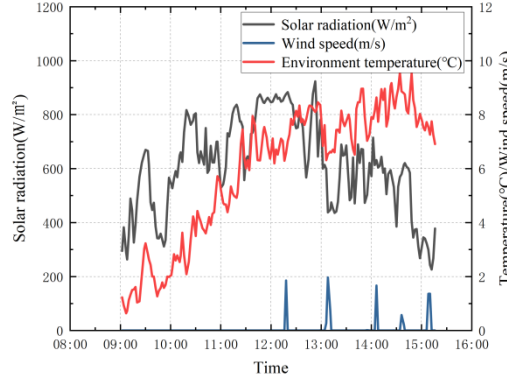


Fig.6 Changes in solar radiation, ambient temperature and ambient wind speed

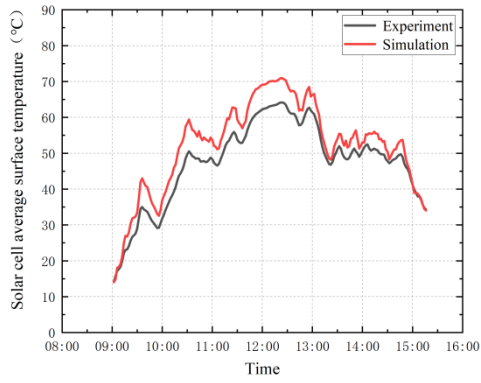


Fig.7 Average surface temperature variation

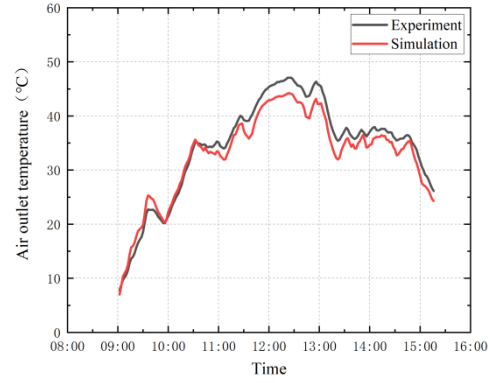


Fig.8 Air outlet temperature variation

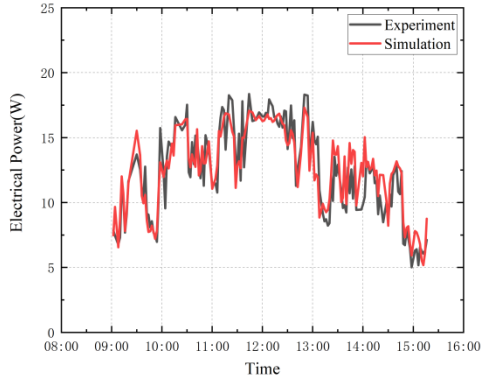


Fig.9 Generating power variation

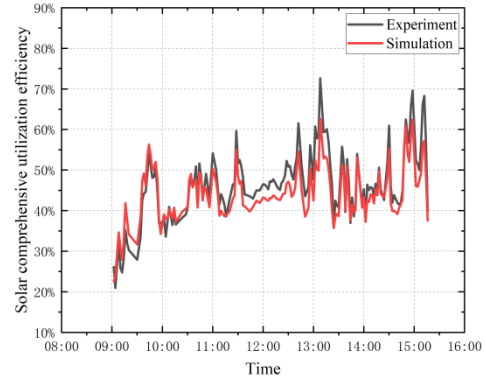


Fig.10 solar comprehensive utilization efficiency variation

Figure 7-10 compares the simulation results and the experimental results of the average surface temperature, air outlet temperature, generating power, and solar comprehensive utilization efficiency of the solar PV/T collector solar cell. This comparison verifies the accuracy of the model. The deviation between simulation and experimental results can be expressed by the root mean square deviation (*RMSD*) and correlation coefficient (*r*). The calculation formula is as follows:

$$RMSD = \sqrt{\frac{1}{n} \sum_{i=1}^n [(X_i - Y_i)]^2} \quad (30)$$

$$r = \frac{\sum_{i=1}^n (X_i - \bar{X})(Y_i - \bar{Y})}{\sqrt{\sum_{i=1}^n (X_i - \bar{X})^2} \sqrt{\sum_{i=1}^n (Y_i - \bar{Y})^2}} \quad (31)$$

Where, X_i is the simulation result of each parameter, and Y_i is the experimental result of each parameter.

Table 3 outlines the experimental and simulation verification results of various parameters, including the average temperature of the collector solar cell surface, air outlet temperature, generating power, and solar comprehensive utilization efficiency. The degree of modeling conformity was evaluated using the root-mean-square deviation and correlation coefficient. The simulation results demonstrate a high level of agreement with the experimental data, affirming the feasibility of the proposed wave plate heat balance calculation method.

Table 3. Experimental and simulation results verify

Parameters	<i>RMSD</i>	<i>r</i>
Average surface temperature	11.12%	0.9875
Air outlet temperature	6.46%	0.9926
Generating power	14.12%	0.9051
Solar comprehensive utilization efficiency	8.38%	0.9345

4 Results and discussion

The solar PV/T air collector's upper channel wave plate and lower channel staggered fin are the key structures that play a crucial role in enhancing the collector's performance. In this section, we use the heat transfer model established earlier to examine the effects of two key structural parameters, namely, the height combination of the upper and lower runners and the fin arrangement of the lower runner, on the photoelectric/photothermal performance of the collector. We simulate the performance of the collector under specific environmental conditions, with an ambient temperature of 2°C, solar irradiation of 800W/m², air flow of 0.014kg/s, ambient wind speed of 0m/s, and collector air inlet temperature of 5°C.

4.1 Upper/lower runner height combination

This section aims to investigate the influence of the combined upper and lower runner height on collector performance. In the study, the total runner height is held constant while the fin interval and row number of the lower runner are fixed. As the flow section of the upper passage undergoes periodic changes due to the presence of wave plates, the integrated average height H_1 is employed to characterize the height of the upper passage.

Table 4. Different upper/lower runner height combination simulation conditions

Conditions	1	2	3	4	5	6	7	8	9	10
Height of upper runner(mm)	29	28	27	26	25	24	23	22	21	20
Height of lower runner(mm)	99	100	101	102	103	104	105	106	107	108

Ten control groups were set in the simulation, as shown in tab.4. The parameters of each data region of the collector were compared after 1 hour of simulation.

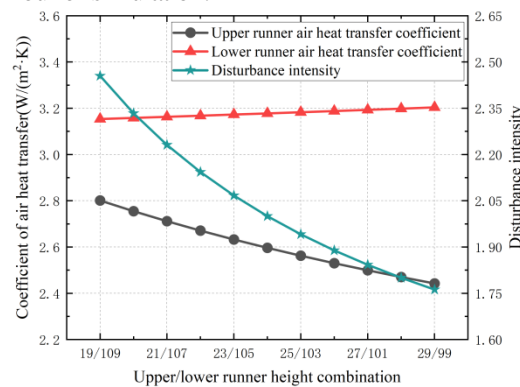


Fig.11 Change of air heat transfer capacity in upper/lower runner

Figure 11 shows the change of air heat transfer capacity of upper/lower runner with the combination of

upper/lower runner height. The figure indicates that when the combination of the upper and lower runner heights is 19mm and 109mm, respectively, the disturbance strength and air heat transfer coefficient of the upper runner are 2.455 and 2.801W/(m²·K), respectively, while the air heat transfer coefficient of the lower runner is 3.153W/(m²·K). Conversely, when the heights of the upper and lower runners are 29mm and 99mm, respectively, the disturbance intensity and air heat transfer coefficient of the upper runner are 1.762 and 2.442W/(m²·K), respectively, while the air heat transfer coefficient of the lower runner is 3.203W/(m²·K).

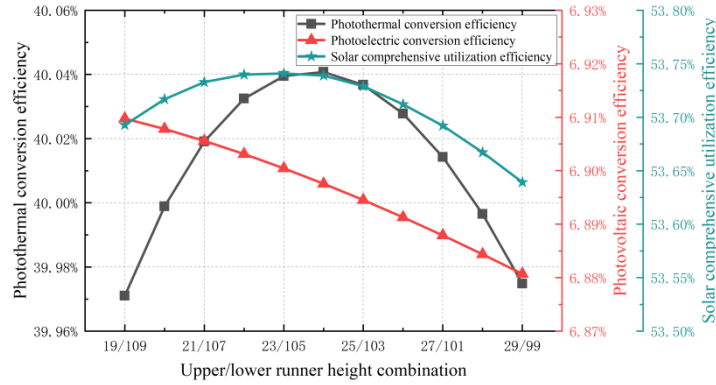


Fig.12 Change of collector efficiency

Figure 12 presents the variation of the collector's photoelectric conversion efficiency, photothermal conversion efficiency, and solar energy comprehensive utilization efficiency concerning the height combination of the upper and lower runners. The figure shows that, as the height combination of the upper/lower runner increases from 19mm/109mm to 29mm/99mm, the photoelectric conversion efficiency declines from 6.91% to 6.881%. When the height combination of the upper/lower runner attains 24mm/104mm, the photothermal conversion efficiency initially increases from 39.971% to 40.041%, then decreases to 39.975%. Similarly, when the height ratio is 23mm/105mm, the comprehensive utilization efficiency of solar energy first rises from 53.693% to 53.741%, then drops to 53.639%. The reduction of the photoelectric conversion efficiency indicates that the overall heat transfer capacity of the air in the collector is reduced. The change of the height combination of the upper and lower channels will affect the airflow distribution of the two channels and lead to the change of the photothermal conversion efficiency.

4.2 Lower runner fin arrangement

The arrangement of fins can be changed by adjusting two key structural parameters, namely equivalent diameter (D_p) and fin row number (z). In the simulation, the height combination of the upper and lower runner of the collector is set at 23mm/105mm, while the equivalent diameter of the rectangular runner and the number of fin rows are manipulated. As the height of the lower runner remains constant, the corresponding fin spacing is calculated to conduct the simulation calculation under the condition of linearly increasing equivalent diameter. The variations in the parameters are documented in tab.5. Subsequently, after a one-hour simulation, the parameters of each data region of the collector are compared to determine the changes.

Table 5. Different equivalent diameters and fin rows simulation conditions

Condition	Equivalent diameters	Spacing of fins	Number of fin rows
s	D_p (mm)	b_p (mm)	z (row)
1	70	53	1-7
2	80	65	1-7
3	90	79	1-7
4	100	96	1-7
5	110	116	1-7
6	120	140	1-7

Figure 13 depicts the impact of these variables on the air heat transfer coefficient in the lower runner. When the equivalent diameter is 70 mm and the number of fin rows increases from 1 to 7, the heat transfer coefficient rises from 2.27 W/(m²·K) to 4.36 W/(m²·K). Similarly, when the equivalent diameter is 120 mm and the number of fin rows increases from 1 to 7, the air heat transfer coefficient increases from 1.89 W/(m²·K) to 3.63 W/(m²·K).

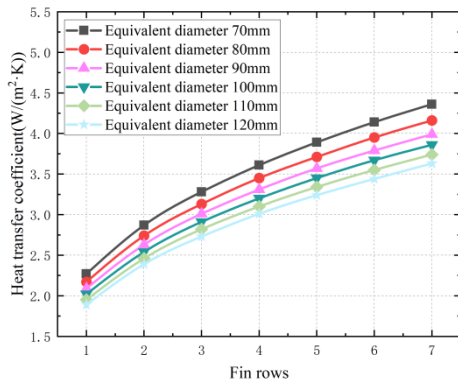


Fig.13 Change of air heat transfer capacity in lower runner

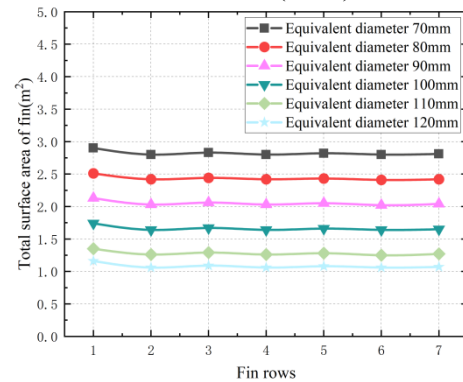


Fig.14 Variation of the total surface area of the fin

Figure 14 displays the total surface area of the fins in response to changes in the equivalent diameter and length of fins. Specifically, an increase in the equivalent diameter leads to a decrease in the number of fins and consequently, a decrease in the total surface area of the fins. Conversely, when the number of fin rows changes, the total surface area of the fins fluctuates within a small range, rendering the influence of the change negligible.

By examining the variations of the total surface area of fins with the equivalent diameter and the number of fin rows in fig.13 and fig.14, it becomes apparent that the total surface area of fins increases by approximately 0.4 m² when the equivalent diameter decreases by 10 mm. This results in a corresponding increase in the air heat transfer coefficient of the lower flow passage, ranging from 0.076 to 0.146 watts per square meter per Kelvin (W/(m²·K)). Conversely, increasing the number of fin rows by one does not significantly impact the total surface area of the fins, with a negligible fluctuation of only about 0.02 m². However, it does result in a substantial increase in the air heat transfer coefficient, ranging from approximately 0.29 to 0.348 W/(m²·K). Therefore, it can be concluded that modifying the fin row number is a more efficient and cost-effective method for enhancing the air heat transfer coefficient of the lower flow passage than altering the equivalent diameter.

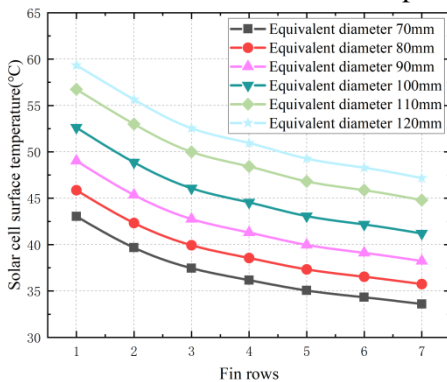


Fig.15 Surface temperature variation of solar cell

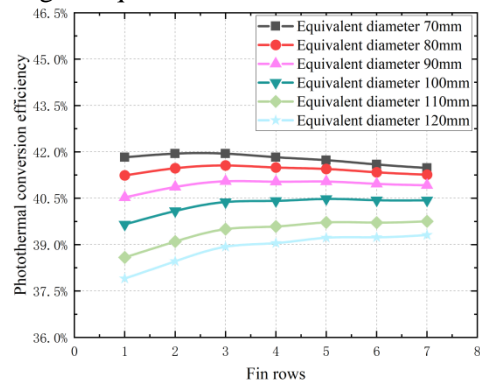


Fig.16 Change of photothermal conversion efficiency

Figure 15 depicts the variation in surface temperature of solar cells with respect to the equivalent diameter and fin row number in the collector. The figure reveals that the surface temperature of the solar cell layer increases with an increase in the equivalent diameter, while a rise in the number of fin rows leads to a decrease in temperature. Notably, the rectangular runner with an equivalent diameter of 70mm and 7 rows of fins yields the lowest temperature of the solar cell layer, which is 33.593°C. When the equivalent diameter and fin row number of the rectangular runner are 120mm and 1, respectively, the temperature of the solar cell layer is 59.333°C.

Figure 16 depicts the relationship between collector photothermal conversion efficiency and two critical parameters, equivalent diameter and fin row number. Notably, when the equivalent diameter of the rectangular channel is 70mm, the photothermal conversion efficiency is optimal. Furthermore, the photothermal conversion efficiency exhibits an upward trend when the number of fin rows increases from one to two, rising from 41.823% to 41.943%. Conversely, as the number of fin rows increases from two to seven, the photothermal conversion efficiency decreases from 41.943% to 41.48%, signaling a downward trend.

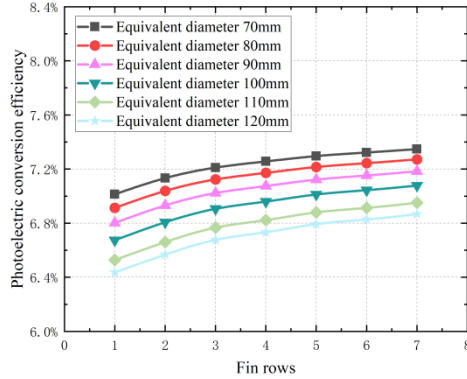


Fig.17 Change of photoelectric conversion efficiency

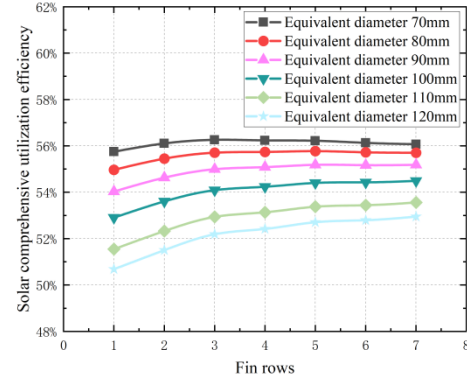


Fig.18 Changes of solar comprehensive utilization efficiency

Figure 17 presents the relationship between collector photoelectric conversion efficiency, equivalent diameter, and fin row number. The maximum efficiency of 7.348% is attained at an equivalent diameter of 70mm and 7 fin rows, while the lowest efficiency of 6.436% is observed at an equivalent diameter of 120mm and a single fin row.

Figure 18 portrays the correlation between collector solar comprehensive utilization efficiency, equivalent diameter, and fin length. As demonstrated by the graphical representation, an increase in the equivalent diameter of the rectangular channel is accompanied by a notable reduction in comprehensive utilization efficiency of solar energy. Furthermore, an initial increase in the comprehensive utilization efficiency of solar energy is observed as the number of fin rows increases, followed by a declining trend that becomes more pronounced as the equivalent diameter increases. Notably, at an equivalent diameter of 70mm and three fin rows, the maximum solar energy comprehensive utilization efficiency reached 56.261%.

4.3 Efficiency comparison

In order to analyze the performance of the optimized solar PV/T collector (Scheme 1), a double-channel solar PV/T collector (Scheme 2) with unequal cross section fins in literature^[15] was taken as the control group to compare and verify the performance advantages of the solar PV/T collector proposed in this paper.

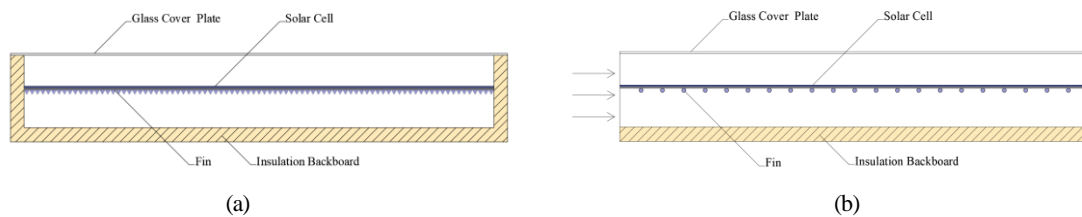


Fig.19 A double-channel solar PV/T collector with unequal cross section fins (Scheme 2): (a) Front view; (b) Side view.

As shown in fig.19, solar PV/T collectors (Scheme 2) is also double-channel structures, and the fins of unequal cross sections are attached to the back of the photovoltaic module in the form of a triangle. The height, width and length of each triangle of the ribs are the same, all of which are 8mm, an

d a total of 125 triangles are installed in one transverse rib. The solar PV/T wind collector is located in Engineering Building 2, Yongtang Campus, Bukyung University, Busan, Korea. The experiment time was from 10:00 to 16:00, and a fixed air flow rate was used for the experiment.

In order to ensure the performance comparison between the two under the same conditions, the experimental conditions and solar cell parameters of Scheme 2 are adopted. The changes of solar irradiation and ambient temperature used in the simulation over time are shown in fig.20. In addition, using the solar cell module in Scheme 2, model Q-PEakBFL-G4.4, the photoelectric conversion efficiency of the solar cell can reach 18.6% under standard test conditions (solar irradiation 1000W/m^2 , module temperature 25°C).

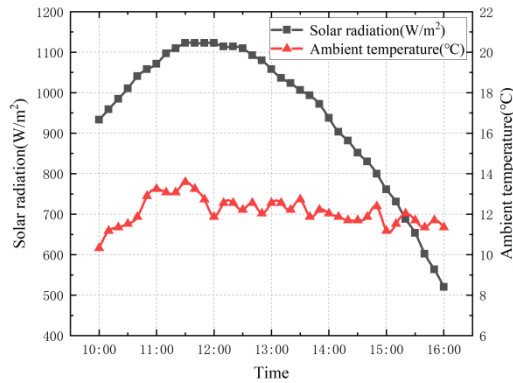


Fig.20 Simulated environmental parameter

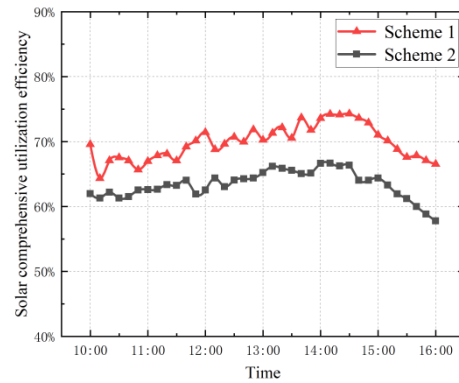


Fig.21 Changes of solar comprehensive utilization efficiency

Figure 21 shows the change of the solar comprehensive utilization efficiency over time for two kinds of solar PV/T collectors. As can be seen from the figure, the all-day average comprehensive solar energy utilization efficiency of scheme 1 is 69.85%, and the maximum comprehensive solar energy utilization efficiency is 74.28%. The average all-day comprehensive solar utilization efficiency of Scheme 2 is 63.39%, and the maximum comprehensive solar utilization efficiency is 66.67%. The comprehensive utilization efficiency of solar energy in scheme 1 is much higher than that in scheme 2, because scheme 1 more effectively improves the heat transfer capacity of air in the flow channel.

5 Conclusion

This paper introduces a novel approach for enhancing the performance of solar photovoltaic-thermal (PV/T) air collectors using staggered fins. In this paper, a heat transfer model of staggered fin solar PV/T air collector is established, and the reliability of the model is verified by experimental results.

In addition, the structure parameters of the collector are studied by means of a model. The results show that the maximum solar comprehensive utilization efficiency is 56.261% when the upper/lower runner height combination is 23mm/105mm at an equivalent diameter of 70 mm and a fin row number of 3. Compared with other collectors, the average comprehensive utilization efficiency of solar energy in the whole day is increased by 8.21% under the same experimental conditions.

Due to the collector heat transfer model in this paper is based on several assumptions, the model needs to be further optimized. In addition, the parameters used in this simulation are mainly environmental parameters in Changchun, Jilin Province, China, and meteorological parameters in other areas need to be introduced to study the efficiency of the collector.

Acknowledgments: The authors acknowledge the support of the Jilin Province Science and Technology Development Plan Project (20220203160SF).

Nomenclature

A	area, [m ²]	Re	Reynolds number
b	width, [m]	$RMSD$	the root mean square deviation
Br	temperature coefficient, [K ⁻¹]	Δt	data acquisition interval, [s]
c	specific heat, [Jkg ⁻¹ K ⁻¹]	T	Temperature, [K]
d	Thickness, [m]	u	heat loss coefficient, [Wm ⁻² K ⁻¹]
D	equivalent diameter, [m]	U	output voltage, [V]
E	electric power, [Wm ⁻²]	v	velocity, [m/s]
G	solar irradiance, [Wm ⁻²]	W	uncertainty
h	coefficient of heat transfer, [Wm ⁻² K ⁻¹]	z	number of fin rows
H	height, [m]	<i>Greek symbols</i>	
I	electric current, [A]	α	absorptance
J	disturbance intensity	ε	emissivity
l	length, [m]	η	transfer efficiency
\dot{m}	air mass flow rate, [kg/s]	λ	heat conductivity coefficient, [Wm ⁻¹ K ⁻¹]
M	quality, [kg]	μ	aerodynamic viscosity, [Pa·s]
n	number of fins	ζ	coverage ratio
Nu	Nushelt number	ρ	density, [kg/m ³]
Pr	Prandtl number	σ	Stefan Boltzmann constant
Q	air volume flow, [m ³ s ⁻¹]	τ	transmittancy
r	correlation coefficient	ν	viscosity coefficient of air motion, [m ² s ⁻¹]

References:

- [1] Kern, E.C., Russell, M.C., Combined photovoltaic and thermal hybrid collector systems, *Proceedings*, 13th IEEE Photovoltaic Specialists, Washington DC, USA, 1978, pp. 1153-1157.
- [2] Fterich, M., et al, Experimental parametric study of a mixed-mode forced convection solar dryer equipped with a PV/T air collector, *Solar Energy*, 171(2018), pp. 751-760. DOI:10.1016/j.solener.2018.06.051.
- [3] Rounis, E.D., et al, Multiple-inlet Building Integrated Photovoltaic/Thermal system modelling under varying wind and temperature conditions, *Solar Energy*, 139(2016), 1, pp. 157-170. DOI:10.1016/j.solener.2016.09.023.
- [4] Ahn, J.G., et al, A Study on Experimental Performance of Air-Type PV/T Collector with HRV, *Energy Procedia*, 78(2015), pp. 3007-3012. DOI:10.1016/j.egypro.2015.11.705.
- [5] Sainthiya, H., Beniwal, N.S., Different types of cooling systems used in photovoltaic module solar system: A review, *Proceedings*, 2017 International Conference on Wireless Communications, Signal Processing and Networking IEEE, Chennai, India, 2017, pp. 1500-1506. DOI:10.1109/WiSPNET.2017.8300012.
- [6] Kumar, R., Rosen, M.A., A critical review of photovoltaic-thermal solar collectors for air heating, *Applied Energy*, 88(2011), 11, pp. 3603-3614. DOI:10.1016/j.apenergy.2011.04.044.
- [7] Pandey, K.M., Chaurasiya, R., A review on analysis and development of solar flat plate collector, *Renewable and Sustainable Energy Reviews*, 67(2017), 67, pp. 641-650. DOI:10.1016/j.rser.2016.09.078.
- [8] Imenes, A.G., Mills, D.R., Spectral beam splitting technology for increased conversion efficiency in solar concentrating systems: a review, *Solar Energy Materials & Solar Cells*, 84(2004), 1-4, pp. 19-69. DOI:10.1016/j.solmat.2004.01.038.

- [9] Kamthania, D., et al, Energy and exergy analysis of a hybrid photovoltaic thermal double pass air collector, *Applied Solar Energy*, 47(2011), 3, pp. 199-206. DOI:10.3103/S0003701X11030066.
- [10] Slimani, M.E.A., et al, A detailed thermal-electrical model of three photovoltaic/thermal (PV/T) hybrid air collectors and photovoltaic (PV) module: Comparative study under Algiers climatic conditions, *Energy Conversion & Management*, 133(2017), pp. 458-476. DOI:10.1016/j.enconman.2016.10.066.
- [11] Ooshaksaraei, P., et al, Performance of four air-based photovoltaic thermal collectors configurations with bifacial solar cells, *Renewable Energy*, 102(2017), pt.B, pp. 279-293. DOI:10.1016/j.renene.2016.10.043.
- [12] Cooper, et al, Development of a dynamic model for a hybrid photovoltaic thermal collector-Solar air heater with fins, *Renewable Energy*, 101(2017), Feb., pp. 816-834.
- [13] Elsafi, A., Gandhidasan, P., Performance of a photovoltaic or thermal double-pass solar air heater with different fin configurations, *Clean Energy Technol*, 3(2015), pp. 28-33. DOI:10.7763/JOCET.2015.V3.163.
- [14] Mojumder, J.C., et al, An experimental investigation on performance analysis of air type photovoltaic thermal collector system integrated with cooling fins design, *Energy & Buildings*, 130(2016), oct., pp. 272-285. DOI:10.1016/j.enbuild.2016.08.040.
- [15] Choi, H.U., Choi, K.H., Performance Evaluation of PV/T Air Collector Having a Single-Pass Double-Flow Air Channel and Non-Uniform Cross-Section Transverse Rib, *Energies*, 13(2020). DOI:10.3390/en13092203.
- [16] Yu, J.S., et al, Effect of Triangular Baffle Arrangement on Heat Transfer Enhancement of Air-Type PVT Collector, *Sustainability*, 12(2020). DOI:10.3390/su12187469.
- [17] Jha, P., et al, An experimental study of a photovoltaic thermal air collector (PVTAC): A comparison of a flat and the wavy collector, *Applied thermal engineering: Design, processes, equipment, economics*, 163(2019).
- [18] Al-Waeli, A.H.A., et al, Modeling and experimental validation of a PVT system using nanofluid coolant and nano-PCM, *Solar Energy*, 117(2019), JAN., pp. 178-191. DOI:10.1016/j.solener.2018.11.016.
- [19] Shan, F., et al, Comparative simulation analyses on dynamic performances of photovoltaic–thermal solar collectors with different configurations, *Energy Conversion & Management*, 87(2014), pp. 778-786. DOI:10.1016/j.enconman.2014.07.077.
- [20] Khelifa, A., et al, Analysis of a Hybrid Solar Collector Photovoltaic Thermal (PVT), *Elsevier Ltd*, 74(2015), pp. 835-843. DOI:10.1016/j.egypro.2015.07.819.
- [21] Ranganathan, S.K., et al, Numerical model and experimental validation of the heat transfer in air cooled solar photovoltaic panel, *Thermal Science*, 20(2016), 4, pp. 1071-1081. DOI:10.2298/TSCI170702161E.
- [22] Othman, M.Y., et al, Performance analysis of PV/T Combi with water and air heating system: An experimental study, *Renewable Energy*, 86(2016), 1, pp. 716-722. DOI:10.1016/j.renene.2015.08.061.
- [23] Wenhua, L., et al, Numerical simulation of flow and heat transfer in rectangular channel with different aspect ratios, *Proceedings, 5th ASME International Conference on Micro/Nanoscale Heat and Mass Transfer*, Biopolis, Singapore, 2016, pp. 1-4. DOI:10.1115/MNHMT2016-6602.
- [24] Chao, G., et al, Numerical simulation and experimental validation of tri-functional

- photovoltaic/thermal solar collector, *Energy*, 87(2015), pp. 1-11. DOI:10.1016/j.energy.2015.05.017.
- [25] Incropera, F. P., Fundamentals of heat and mass transfer, Wiley, 2006. DOI:US5328671 A.
- [26] Sohel, M.I., et al, A dynamic model for air-based photovoltaic thermal systems working under real operating conditions, *Appl Energy*, 132(2014), pp. 216-225. DOI:10.1016/j.apenergy.2014.07.010.
- [27] Aste, N., et al, Performance monitoring and modeling of an uncovered photovoltaic-thermal (PVT) water collector, *Solar Energy*, 135(2016), pp. 551-568. DOI:10.1016/j.solener.2016.06.029.
- [28] Tiwari, A., et al, Performance evaluation of photovoltaic thermal solar air collector for composite climate of India, *Solar Energy Materials & Solar Cells*, 90(2006), 2, pp. 175-189. DOI:10.1016/j.solmat.2005.03.002.
- [29] Li, Z., Gao, Y., Numerical study of turbulent flow and heat transfer in cross-corrugated triangular ducts with delta-shaped baffles, *International Journal of Heat and Mass Transfer*, 108(2017), pp. 658-670. DOI:10.1016/j.ijheatmasstransfer.2016.12.054.
- [30] Yuan, W., et al, Comparison study of the performance of two kinds of photovoltaic/thermal(PV/T) systems and a PV module at high ambient temperature, *Energy*, 148(2018), APR.1, pp. 1153-1161. DOI:10.1016/j.energy.2018.01.121.

RECEIVED DATE: 9.4.2023.
 DATE OF CORRECTED PAPER: 21.6.2023.
 DATE OF ACCEPTED PAPER: 26.7.2023.